Experimental study of three-wave interactions among capillary-gravity surface waves

Florence Haudin,[1] Annette Cazaubiel,[1,2] Luc Deike,[3] Timothée Jamin,[1] Eric Falcon,[1] and Michael Berhanu[1]
[1]*Université Paris Diderot, Sorbonne Paris Cité, MSC, CNRS (UMR 7057), 75013 Paris, France*
[2]*Ecole Normale Supérieure, Département de Physique, 75005 Paris, France*
[3]*Scripps Institution of Oceanography, University of California San Diego, San Diego, California 92093, USA*
(Received 11 January 2016; published 11 April 2016)

In propagating wave systems, three- or four-wave resonant interactions constitute a classical nonlinear mechanism exchanging energy between the different scales. Here we investigate three-wave interactions for gravity-capillary surface waves in a closed laboratory tank. We generate two crossing wave trains and we study their interaction. Using two optical methods, a local one (laser doppler vibrometry) and a spatiotemporal one (diffusive light photography), a third wave of smaller amplitude is detected, verifying the three-wave resonance conditions in frequency and in wave number. Furthermore, by focusing on the stationary regime and by taking into account viscous dissipation, we directly estimate the growth rate of the resonant mode. The latter is then compared to the predictions of the weakly nonlinear triadic resonance interaction theory. The obtained results confirm qualitatively and extend previous experimental results obtained only for collinear wave trains. Finally, we discuss the relevance of three-wave interaction mechanisms in recent experiments studying gravity-capillary turbulence.

DOI: 10.1103/PhysRevE.93.043110

I. INTRODUCTION

When a wave field is governed by linear propagation equations, the different space and time scales coupled by the dispersion relation evolve independently. In contrast, by introducing nonlinearity, energy exchanges between the scales become possible. Among nonlinear interaction phenomena, particular attention has been given to the resonant interaction mechanisms [1–3]. In the weakly nonlinear limit, dispersive waves can substantially exchange energy at long time, if their respective angular frequencies $\omega_i = 2\pi\ f_i$ and wave numbers $\mathbf{k_i}$ ($\|\mathbf{k_i}\| = k_i = \frac{2\pi}{\lambda_i}$) satisfy the resonance conditions. For a process involving N waves, these conditions take the form:

$$\mathbf{k_1} \pm \mathbf{k_2} + \cdots \pm \mathbf{k_N} = 0 \tag{1}$$

$$\omega(\mathbf{k_1}) \pm \omega(\mathbf{k_2}) + \cdots \pm \omega(\mathbf{k_N}) = 0 \tag{2}$$

with $\omega(\mathbf{k_i})$ the dispersion relation of the waves.

At the lowest order of the weakly nonlinear expansion, three-wave mechanism or triadic resonance is usually considered for a system with a quadratic nonlinearity. Nevertheless, if the dispersion relation cannot satisfy the three-wave resonance condition, four-wave mechanism occurs. This is precisely the case of large-scale surface gravity waves [4,5], in which resonant interactions rule dynamics and evolution of oceanic gravity waves [6]. At smaller scales, in the crossover between gravity and capillary waves and also for pure capillary waves, three-wave interactions occur [7]. Triadic resonance is also involved in numerous natural and physical examples in which they mediate energy exchanges between the different scales, such as internal gravity waves [8] in oceanography or for three-wave mixing in nonlinear optics [9]. Recent experiments have indeed investigated triadic resonance and verified the resonance condition in internal waves [10], in inertial waves in rotating tank [11], in plasma waves [12], or in hydroelastic waves [13].

Moreover, understanding resonant interaction mechanisms is of prime interest in the study of wave turbulence regimes. The dynamics of a set of numerous random waves in interaction, is said to be in a wave turbulence regime, when a self-similar mechanism transfers energy from an injection scale to a dissipative scale. The aim of the weak turbulence theory [14,15] is to describe this regime by taking the main wave resonant mechanism as the elemental process coupling the waves. Power spectra of wave amplitude can be analytically derived as power laws of k (spatial spectrum) or ω (temporal spectrum). Recently several laboratory investigations of wave turbulence have been carried out in regard of weak turbulence theory, specifically for the example of hydrodynamics surface waves. At large scale, in the gravity wave regime involving four-wave interactions, power spectra of wave elevation are generally in partial agreement with theoretical predictions. The exponent of the scale-power law depends on forcing amplitude and seems to saturate close to the predicted value [16–18]. At small scale, in the capillary wave regime, several independent studies report, in contrast, observation of the exponents given by the weak turbulence theory [18–23]. More recently the spatiotemporal characterization of capillary wave turbulence [24] and the study of its decay [25] have shown that despite the compatibility of the spectra with weak turbulence theory, the needed experimental conditions depart from the theoretical framework. First, viscous dissipation occurs at all the scales of the turbulent cascade leading to a nonconserved energy flux [26] and anisotropy in the forcing is conserved [24]. Then the dimensionless nonlinear parameter, i.e., the wave steepness, seems too large to verify the hypothesis of small nonlinearity, needed to consider resonant interactions. Therefore, in order to solve this paradox, an experimental investigation of three-wave resonant interactions of gravity-capillary surface waves is here performed, with similar experimental conditions than those exhibiting capillary wave turbulence.

Although this phenomenon has been widely studied, some important features have never been tested experimentally. Theoretically, by considering three waves verifying the resonant condition, amplitude equations can be derived using

perturbative [7,27] or variational [28] methods, in which dissipation is neglected. A few experimental studies tried to verify these last results in laboratory channel tanks, by generating a well-controlled sinusoidal wave train. The first investigations of such interactions were performed in the 1970s for a special degenerate case, the Wilton ripples ($f_1 = f_2 =$ 9.8 Hz, $f_3 = 19.6$ Hz for pure water) with, in that case, the daughter wave collinear to the two mother waves [29]. By adding dissipation as a perturbation, a conclusive agreement was found with theory. Similar experiments observed the same phenomenon under near-resonant conditions [30]. Then subharmonic generation of gravity-capillary waves were also studied at the beginning of the 1980s [31], in which two waves are generated from a single one at higher frequency. However, this three-wave process was not properly observed due to occurrence of subharmonic cross waves [3,32]. At the end of the 1980s, the subharmonic three-wave interaction phenomenon was appropriately reported [33–35], by demonstrating the instability of a capillary surface wave train, whose frequency is above 19.6 Hz. The selection process of the observed triads was also studied. Moreover, in a wave turbulence regime, a recent experimental study close to the gravity-capillary crossover has shown significant occurrence of quasi-one-dimensional three-wave interactions [36]. Finally, occurrence of three-wave interactions was demonstrated for capillary waves under parametric excitation [37].

In that context, the present paper investigates interactions between two gravity-capillary mother waves and a third daughter wave. By studying experimentally interactions between two sinusoidal wave trains producing a daughter wave at higher frequency, we intend to characterize the elemental process of wave turbulence, producing a positive transfer of energy through the small scales. This regime is indeed formed by a dynamic superposition of multiple interactions. In particular we aim to test the robustness of resonant interaction mechanisms knowing that in small-scale experiment viscous dissipation is significant, multiple reflections occur, and time-scale separation is not guaranteed allowing observation of nonresonant interactions [6,30]. Moreover, three-wave interaction mechanisms for surface waves have never been addressed experimentally in the configuration where two mother waves generate one daughter wave at higher frequency. Only the degenerated and collinear case [29,30] ($f_1 = f_2$; $f_3 = 2f_1$) and the subharmonic generation of two waves by one wave at high frequency [31–33] ($f_1 = 2f^*$; $f_2 = f_3 = f^*$) have been experimentally investigated.

The paper is organized as follows. A state of the art is given in Sec. I on the topics of gravity-capillary wave interactions whereas Sec. II recalls the key points of the theoretical background of the resonant triadic interactions. Section III presents the experimental setup and techniques. Section IV reports an extensive study with local and spatial measurements of the triad, where two mother waves of frequency $f_1 = 15$ and $f_2 = 18$ Hz generate a daughter wave at the frequency $f_3 = f_1 + f_2 = 33$ Hz. Section V shortly extend the results to another triad experimentally tested ($f_1 = 16$, $f_2 = 23$, $f_3 =$ 39 Hz) and draws some conclusions. Finally, in the Appendix, characterization of wave dissipation in the experimental setup is given.

II. THREE-WAVE RESONANCE: THEORETICAL BACKGROUND

A. Resonance conditions

Let us consider the case of two mother waves with frequencies f_1 and f_2 and wave vectors $\mathbf{k_1}$ and $\mathbf{k_2}$, leading to the appearance of a daughter wave with frequency $f_3 = f_1 + f_2$.

Each wave i satisfies the gravity-capillary linear dispersion relation:

$$\omega_i^2 = \left[g\, k_i + \frac{\sigma}{\rho} k_i^3 \right] \tanh(k_i\, h_0) \tag{3}$$

with g the gravity acceleration, ρ the fluid density, σ the surface tension and h_0 the liquid depth at rest. As the frequencies are imposed, norms of wave vectors k_i are known by inverting numerically the relation dispersion. The components of the triad satisfy the resonance conditions:

$$\omega_1 + \omega_2 = \omega_3 \quad \mathbf{k_1} + \mathbf{k_2} = \mathbf{k_3}. \tag{4}$$

The angle between the two mother wave vectors $\mathbf{k_1}$ and $\mathbf{k_2}$ is called α_{12}. In the resonance conditions [Eq. (4)], this angle noted $\alpha_{12\,r}$ is completely determined by the choice of mother wave frequencies f_1 and f_2.

$$\cos(\alpha_{12\,r}) = \frac{k_3^2 - \left(k_1^2 + k_2^2\right)}{2k_1k_2}. \tag{5}$$

For the triads, we have investigated in the following, the values of $\alpha_{12\,r}$ are 54 deg ($f_1 = 15$, $f_2 = 18$, and $f_3 = 33$ Hz) and 59 deg ($f_1 = 16$, $f_2 = 23$, and $f_3 = 39$ Hz), by taking $\sigma = 60$ mN/m and $\rho = 1000$ kg/m^3 for water as working fluid. These frequencies belong to the capillary waves domain, but gravity is not negligible and the complete form of the dispersion relation of Eq. (3) has to be used. A schematic view of the wave beams of the mother waves and the resulting interaction zone area are given in Fig. 1(a), with the corresponding angle $\alpha_{12\,r}$ between $\mathbf{k_1}$ and $\mathbf{k_2}$. An origin O and an axis O_ξ in the direction of $\mathbf{k_1} + \mathbf{k_2}$ are defined to

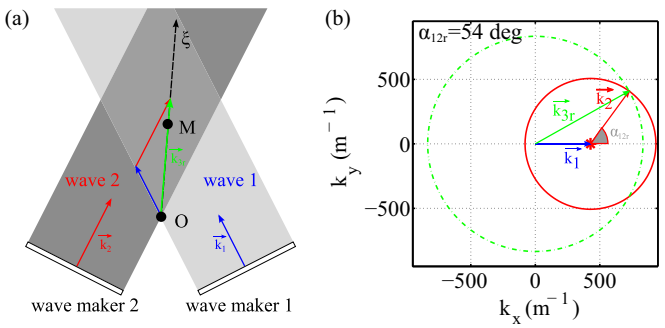

FIG. 1. (a) Schematic view of the interaction zone between the two mother waves. O is the origin of this zone, M locates a point in this area along the direction O_ξ given by $\mathbf{k_1} + \mathbf{k_2}$. (b) Graphical construction of the triad for $f_1 = 15$ Hz and $f_2 = 18$ Hz with $\alpha_{12\,r} = 54$ deg (resonant angle). The green circle (dash-dotted line) corresponds to $\mathbf{k_3 r}$ satisfying the gravity-capillary dispersion relation and the red circle (continuous line) to all location of the extremity of vector $\mathbf{k_2}$. Axes are here defined relatively to $\mathbf{k_1}$.

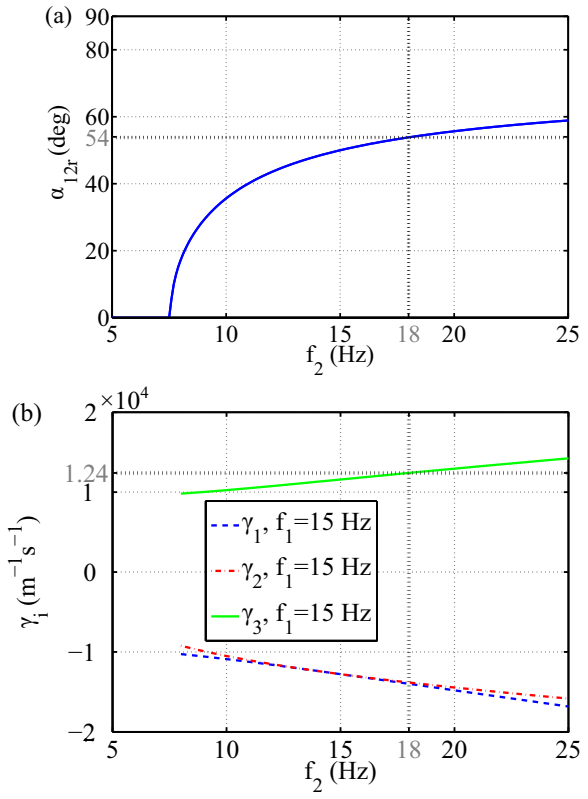

FIG. 2. For a fixed mother wave $f_1 = 15$ Hz, (a) evolution of the angle α_{12r} versus f_2 from Eq. (5) and (b) evolution of the interaction coefficients versus f_2 from Eq. (8).

describe the daughter wave propagation at a given point M along O_ξ.

It is also possible to determine graphically the resonant wave vector $\mathbf{k_{3r}}$ satisfying both the dispersion relation and the resonance conditions as illustrated in Fig. 1(b). The red circle (continuous line) defines the loci of all the possible $\mathbf{k_3}$ built by the sum of $\mathbf{k_1} + \mathbf{k_2}$, different angles between them being possible when changing the orientation of the vector $\mathbf{k_2}$ on this circle, keeping its norm k_2 constant. The green circle (dash-dotted line) corresponds to the loci of the vectors $\mathbf{k_{3r}}$ in accordance with the dispersion relation. As a consequence the intersection between the red and the green circles defines the vector $\mathbf{k_{3r}}$ satisfying both the resonance conditions and the relation dispersion. Two solutions exist corresponding to opposite values of α_{12r}. If the angle between $\mathbf{k_1}$ and $\mathbf{k_2}$ differs from α_{12r}, being for example 90 deg, there is no intersection with the green circle and hence the corresponding triad is not satisfying the dispersion relation anymore. Moreover, varying f_2 for a given f_1 changes the value of α_{12r} computed with Eq. (5). Figure 2(a) shows indeed a significant increase. At the lowest possible value of f_2, $\alpha_{12r} = 0$ and the mother waves are collinear. The value $\alpha_{12r} = 90$ deg, cannot be reached and corresponds to f_2 going to infinity. Note also that another graphical determination of triads is provided by the construction of Simmons [28], which builds in the three-dimensional (3D) space (k_x, k_y, ω) the loci of the vector k_i to be in the resonant situation.

TABLE I. Norms of the wave vectors and interaction coefficients calculated from Eq. (8). The different values are calculated with $\sigma = 60$ mN/m and $\rho = 1000$ kg m^{-3}.

	k_i (m^{-1})	γ_i (m^{-1} s^{-1})
$f_1 = 15$ Hz	428	-1.40×10^4
$f_2 = 18$ Hz	507	-1.38×10^4
$f_3 = 33$ Hz	834	1.24×10^4
$f_1 = 16$ Hz	455	-1.65×10^5
$f_2 = 23$ Hz	626	-1.58×10^4
$f_3 = 39$ Hz	946	1.41×10^4

B. Amplitude equations

In the weakly nonlinear regime, considering one isolated triad, equations can be derived for the amplitudes and the phases of the three waves [28]. By hypothesis, the free surface elevation η is written as the sum of the components of the triad taken as propagative waves: $\eta(x,y,t) = \sum_{i=1}^{3} a_i \cos(\mathbf{k_i}\cdot\mathbf{x} - \omega_i t + \phi_i)$, where a_i and ϕ_i are the amplitude and the phase of the wave i. Temporal evolutions of a_i and ϕ_i are then expressed as a system of six coupled first-order linear differential equations. Moreover, in capillary wave experiments wave dissipation due to viscosity needs to be taken into account. Considering a linear dissipation process, amplitude equations are modified by adding a decay term $\delta_i a_i$ [29,33], where δ_i is the viscous dissipation coefficient, i.e., the inverse of the viscous decay time at the frequency f_i. This approach is justified, if this later time scale is small compared to the characteristic nonlinear time associated with the nonlinear growth of a_3. Then for each component i of the triad, one has [33]:

$$\partial a_i/\partial t + \delta_i a_i + (\mathbf{v}_{gi}.\nabla)a_i = a_{i+1}a_{i+2}\,\gamma_i \sin\phi \qquad (6)$$

$$\partial \phi_i/\partial t + (\mathbf{v}_{gi}.\nabla)\phi_i = \frac{a_{i+1}a_{i+2}}{a_i}\,\gamma_i \cos\phi \qquad (7)$$

with $i = 1,2,3$ interchanged cyclically, ϕ the total phase defined as $\phi = \phi_1 + \phi_2 - \phi_3$, $\nabla = (\partial_x, \partial_y)$, $\mathbf{v}_{gi} = \partial\omega_i/\partial\mathbf{k_i}$ group velocities, and γ_i the interaction coefficients, whose expressions are given by [28]:

$$\gamma_i = -\frac{k_i}{4\omega_i}\sum_{j=1}^{3}\omega_j\omega_{j+1}\left(1 + \frac{\mathbf{k_j}.\mathbf{k_{j+1}}}{k_j k_{j+1}}\right). \qquad (8)$$

In this last formula, the convention of negative frequency for ω_3 is taken in order to write the resonance conditions: $\omega_1 + \omega_2 + \omega_3 = 0$ and $\mathbf{k_1} + \mathbf{k_2} + \mathbf{k_3} = 0$, as defined in the variational derivation of interaction coefficients [28]. In the following except in the calculation of these coefficients, frequencies are considered positive.

In order to provide some orders of magnitude, the evolution of the various γ_i versus f_2 have been plotted on Fig. 2(b), for a fixed value of $f_1 = 15$ Hz. The evolution with f_2 is monotonous (decreasing for $\gamma_{1,2}$ increasing for γ_3). The values of γ_i for (15, 18, 33) and (16, 23, 39) (shortly discussed in Sec. V) are reported in Table I.

The coefficients of the mother waves are negative whereas the coefficient for the daughter wave is positive. The wave

3, initially null, would thus grow, by pumping energy from the waves 1 and 2. With negligible dissipation, a_3 is supposed to grow linearly in time, at short time, as long as $a_3 \ll \sqrt{a_1 a_2}$. Long-time behavior of the system formed by Eqs. (6) and (7) predicts nonlinear oscillations and recurrence phenomena [2,28], also with negligible dissipation.

To make a quantitative comparison between these theoretical results and the following experimental measurements, we study the behavior of the daughter wave with the hypothesis $a_3 \ll \sqrt{a_1 a_2}$. We consider in stationary regime the evolution of the wave amplitude a_3 in the direction O_ξ given by $\mathbf{k_3}$, as previously explained and illustrated in Fig. 1(a). From Eq. (6), we get a linear differential equation of order one with a second member:

$$v_{g3}\, \partial a_3/\partial \xi = -\delta_3 a_3 + a_1 a_2\, \gamma_3 \sin\phi. \tag{9}$$

If the wave field can be considered homogeneous and if the total phase ϕ does not vary with ξ, the previous equation can be integrated and by introducing the coordinate ξ_0 where $a_3(\xi_0) = 0$, we obtain:

$$a_3(\xi) = \frac{\gamma_3 \sin\phi}{\delta_3} a_1 a_2 \left[1 - \exp\left(-\frac{\delta_3}{v_{g3}}(\xi - \xi_0)\right)\right]. \tag{10}$$

To be consistent $\partial\phi_3/\partial\xi = 0$, then Eq. (7) imposes $\cos\phi = 0$ and thus $\sin\phi = \pm 1$ or $\phi = \pm\frac{\pi}{2}$. The phase locking at $\phi = \pi/2$ was supposed in most of the experimental studies of three-wave resonance [29,33] and was justified by a reasoning of maximal energy transfer. Otherwise the phase ϕ_3 would be spatially modulated and an analytical solution cannot be expressed any more. The dependency of a_3 with the distance ξ_M from the origin, ξ_0, is expressed by the prefactor K, whose expression is:

$$K(\xi_M) = 1 - \exp\left(-\frac{\delta_3}{v_{g3}}\xi_M\right). \tag{11}$$

As a consequence, at a given point M, a_3 is expected to be proportional to the product $a_1 a_2$ and the slope can be identified to $\gamma_3 \sin\phi\, K(\xi_M)/\delta_3$. In the experiments, ξ_0 is assumed to be at the first crossing point between the two mother wave trains, in the direction of the daughter wave, i.e., the origin point O in Fig. 1(a). As a remark for surface gravity waves, to validate the four-wave resonant mechanism, experiments were performed by generating two distinct waves trains crossing perpendicularly [38,39]. These experiments with negligible dissipation, validated four-wave resonant interaction in the degenerated case [5], in finite wave basins. Similarly, the beginning of the daughter wave is taken at the first crossing point between the two mother wave trains.

Homogeneity of the wave field is hard to fulfill due to viscous dissipation and presence of boundaries, but it will be shown in the following that by taking into account this correction with $K(\xi_M)$, we obtain a satisfying estimation of the interaction parameter γ_3. Moreover, two limit behaviors can be deduced from Eq. (10). At short distance or for weak dissipation, a_3 grows linearly with ξ:

$$a_{3\,\mathrm{lin}}(\xi) = \frac{\gamma_3 \sin\phi}{v_{g3}} a_1 a_2 (\xi - \xi_0). \tag{12}$$

In contrast, at high enough distance, if the amplitude of mother waves remain constant, viscous dissipation can saturate the resonant interaction to a constant value:

$$a_{3\,\mathrm{sat}}(\xi) = \frac{\gamma_3 \sin\phi}{\delta_3} a_1 a_2. \tag{13}$$

Thus, a_3 grows with the distance to reach this saturation value due to the balance between nonlinear growth and viscous dissipation. In contrast to the theory that considers an open system, in this work, we investigate three-wave resonance in a closed system, which is the relevant case for capillary wave turbulence experiments. The circular boundaries of the tank reflect indeed a part of incident waves in many directions. The wave field contains thus a propagative part and a standing (or stationary) part, and this later brings inhomogeneity. In the following, we will show that although effects of reflections are significant, they do not modify the three-wave interaction mechanisms. Thus, reflections present in all closed tanks are not preventing resonant interactions, but make their analysis more complex.

III. EXPERIMENTAL SETUP

We use a circular Plexiglas (PMMA) container of diameter 240 mm filled with a liquid up to a height $h_0 = 50$ mm, corresponding to deep water wave regimes, for frequencies considered in the following. Two gravity-capillary waves 1 ($\mathbf{k_1}$,ω_1) and 2 ($\mathbf{k_2}$,ω_2) are produced at the air-liquid interface using two wave makers, consisting in two vertical rectangular plastic paddles of width 100 mm driven horizontally and independently by two electromagnetic shakers (Brüel & Kjaer LDS V201). The paddles are immersed 10 mm under the surface of the liquid. Recording of the input excitation is carried out by accelerometers (Brüel & Kjaer 4393) glued on the paddles. Note also that the distance and the angle between the two wave makers can be tuned.

Two optical techniques have been used to investigate the wave field: local measurements with a laser Doppler vibrometer and spatiotemporal measurements using the diffusing light photography (DLP) method. The laser Doppler vibrometer (Polytech OPV 506), measures the velocity at one point of the free surface given by the position of the vertical laser beam. The distilled water is white dyed thanks to TiO_2 pigment (Kronos 1001, 10 g in 1 L of water), to make the fluid opaque. The laser beam is thus subjected to a diffuse reflection and the velocity of the point at the free surface is extracted from the interference between incident beam and back-scattered light. After temporal integration, vibrometer can capture deformations smaller than 1 μm, without any bias. For these concentrations of TiO_2, the properties of pure water at ambient temperature (25 °C) are weakly modified. We measure a density ratio with water $\rho_{\mathrm{sol\,TiO_2}}/\rho_{\mathrm{water}} = 1.009$ and a kinematic viscosity $\nu = 1.02 \times 10^{-6}\ \mathrm{m^2\ s^{-1}}$ using a Anton Paar, MCR 500 rheometer, equipped with a cone-plate combination (diameter 50 mm, angle 1 deg). As TiO_2 particles are not accumulating at the interface, surface properties are comparable to those of pure water [40]. By measuring the phase velocity in monochromatic experiments, we find a surface tension of $\sigma = 62 \pm 5$ mN m^{-1}. In the following, measurement point is located at a distance of 90 ± 5 mm from each wave maker, corresponding to the position (x_v, y_v). Figure 3(a) shows a top view of the tank for an angle α_{12}

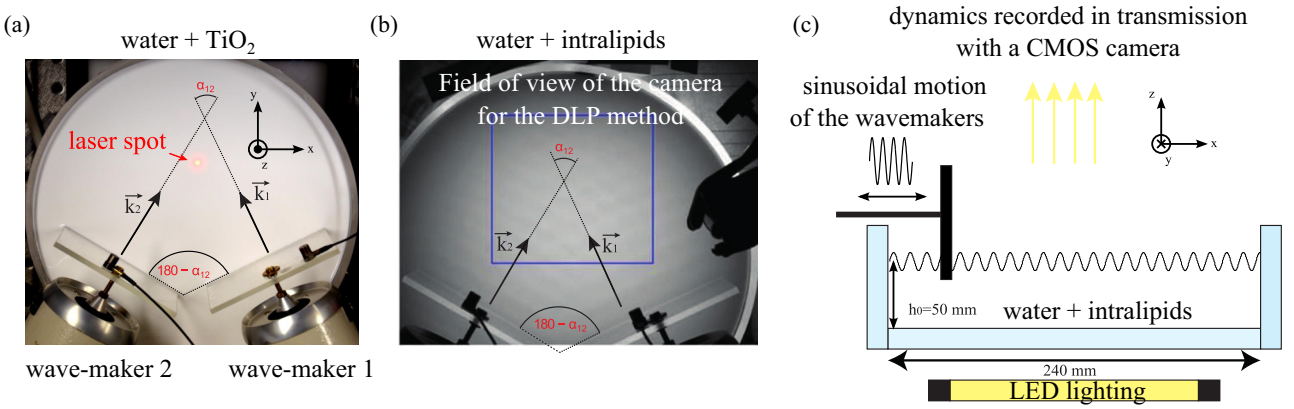

FIG. 3. (a) Top view of the set up for local temporal measurements: the tank is filled with water mixed with TiO_2 pigment. The red spot is the beam of the laser vibrometer. (b) Top view of the setup for spatiotemporal measurements with the DLP method. The liquid is a solution of intralipids in water. The blue rectangle depicts the observation area $\mathcal{S}$ of 103×94 mm^2 where the wave field reconstruction is performed. (c) Schematic representation of the side view of the setup for DLP spatiotemporal measurements.

equal to 60 deg, for experiments using the laser Doppler vibrometer placed about 64 cm above the liquid surface. As a remark, during preliminary experiments, local measurements were performed using a capacitive wave probe, providing very similar results. Attenuation measurements giving values of the viscous damping coefficients δ_i are presented in the Appendix.

The second method, diffusing light photography (DLP) [19], consists in the reconstruction of the 3D free surface from the measurement of the transmitted light through a liquid diffusing the light. A small amount of micrometric particles are added to the liquid (4.5 mL of Intralipids 20% Fresenius Kabi^{TM} in 1 L of distilled water). We measure a density ratio with water $\rho_{\text{sol intra}}/\rho_{\text{water}} = 1.001$ and a kinematic viscosity $\nu = 1.24 \times 10^{-6}$m^2 s^{-1}. The surface tension will be deduced from the measurements. As displayed in Fig. 3(c) a diffuse LED light source of 200×200 mm^2 (Phlox) provides a homogeneous lighting below the transparent tank. Transmitted light is recorded on an observation area $\mathcal{S}$ of 103×94 mm^2, with a fast camera (PCO Edge, scientific CMOS) located above the tank, and with focus made on the surface (frame rate 200 Hz). Knowing that the transmitted intensity is related to the local height of liquid, it is possible with a suitable calibration to reconstruct the wave field in space and time. More details about DLP are available in an experimental work on capillary wave turbulence [24], where a similar setup was used. Spatiotemporal dynamics of free-surface elevation can be thus extracted with a good sensitivity even for steep deformation. This method has an accuracy of order $10\,\mu$m due to uncertainties in the calibration process, and is thus less precise than the laser Doppler vibrometry. Moreover, surfactants present for stabilization purpose in commercial solutions of intralipids increase slightly wave dissipation (see Appendix). Therefore, for quantitative measurements of wave amplitudes, laser Doppler vibrometry will be preferred in the following. However, we have checked that all the phenomena observed with the vibrometer are reproduced with the DLP method with less accuracy and slightly different physical constants. DLP will thus succeed to characterize spatial properties of the wave field and to display mechanisms of three-wave resonant interactions.

Finally, a data acquisition card (NI-USB 6212) controlled through MATLAB^{TM}, sends programmed signals to the electromagnetic shakers and record analog signals from the laser Doppler vibrometer and from the two accelerometers (sampling frequency of 10 kHz). As optical properties of liquid are different for the two methods (opaque for the vibrometry and light diffusing for the DLP), local and spatiotemporal measurements are taken separately on dedicated experiments. For the local measurements, recordings are taken during 170 s, in which waves are generated for 150 s including transient, stationary, and decaying regimes. Each measurement is repeated 12 times to ensure a statistical averaging. Then, for spatiotemporal measurements, due to the larger amount of data, the wave reconstruction is performed usually on a duration of 20.5 s, in stationary regime. Throughout the text, the mother wave amplitudes a_1 and a_2 measured with the vibrometer (wave amplitudes are obtained by bandpass filtering around f_1 and f_2, see Sec. IV D) will be attributed to the spatiotemporal measurement as forcing parameters, which have the same values of forcing amplitude imposed to the electromagnetic shaker. Using this scale, the two kinds of measurements can be compared with a parameter corresponding to properties of the wave field.

IV. EXPERIMENTAL STUDY

We first investigate three-wave interactions, by setting experimentally the conditions imposed by the resonance condition and the dispersion relation. Here we report the results for $f_1 = 15$ and $f_2 = 18$ Hz, imposing the angle $\alpha_{12\,r} = 54$ deg from Eq. (5), between the two wave trains. Appearance of a third wave at the frequency $f_3 = f_1 + f_2 = 33$ Hz is thus expected. The two wave trains are generated by the sinusoidal motion of each paddle. The angle between the two paddles is set at $180 - 54 = 126$ deg with an experimental accuracy estimated to be ±2 deg. Examples of the wave field obtained with DLP measurements, in the transient and the stationary regimes, are displayed in Fig. 4. In the interaction zone between the two mother waves, a modulated wave field is observed, with crests and troughs in the surface height distribution, corresponding mainly to the linear superposition

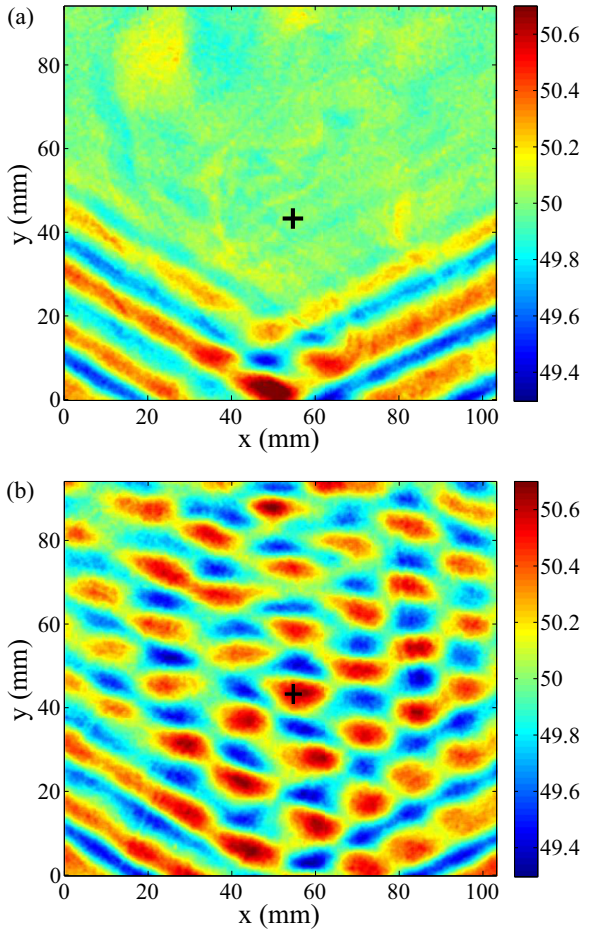

FIG. 4. Examples of wave-field reconstruction obtained with the DLP technique, for $f_1 = 15$ Hz, $f_2 = 18$ Hz and $\alpha_{12} = 54$ deg: (a) in the transient and (b) in the stationary regime, with a color scale in mm (total height of fluid in the tank), with $a_1 = 130$ and $a_2 = 132$ μm (high forcing). The position of the laser spot for vibrometer measurements is indicated by the black cross symbol located at $x_v = 54.6$ mm and $y_v = 43.3$ mm.

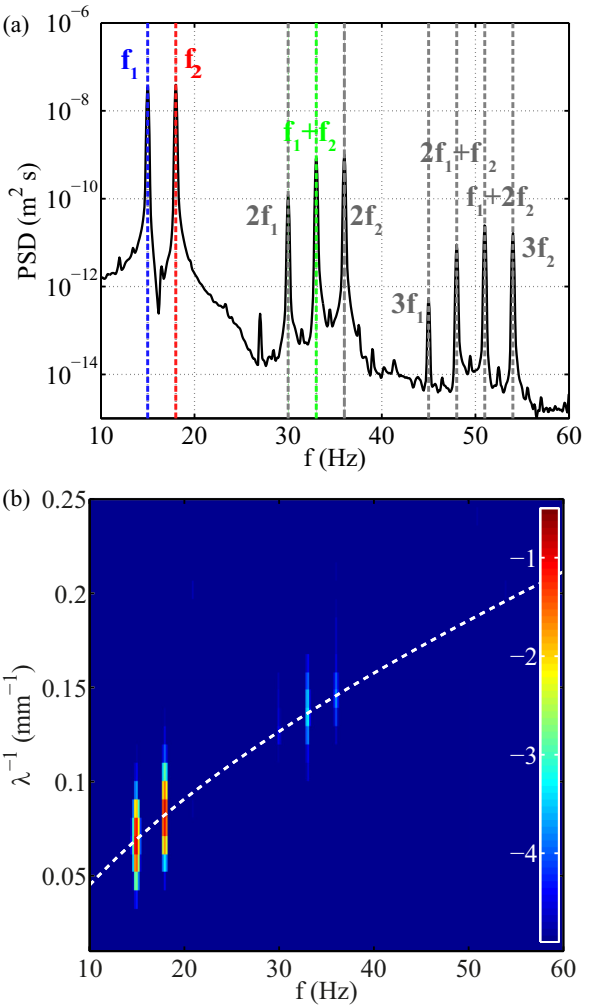

FIG. 5. (a) Local power spectrum $P_\eta(\omega)$ for $f_1 = 15$, $f_2 = 18$ Hz and $\alpha_{12} = 54$ deg. There, $a_1 = 130$ and $a_2 = 132$ μm (high forcing). (b) Spatiotemporal spectrum of wave elevation $S_\eta(\omega,k)$. White dashed line: linear theoretical dispersion relation for $\sigma_{\text{fit}} = 55$ mN/m. Color scale corresponds to $\log_{10}[S_\eta(\omega,k)]$ with S_η in mm^3 s, with $a_1 = 55$ and $a_2 = 56$ μm (low forcing).

of the two mother waves. To detect the presence of the daughter wave, performing a Fourier transform analysis is necessary. From DLP measurements, spatial homogeneity can be also estimated by computing the ratio between the spatial standard deviation of wave amplitude and the spatial average wave amplitude and typical values of 10% are found. The control parameters will be the amplitudes of mother waves a_1 and a_2.

A. Power spectra of wave elevation

We detect the presence of the daughter wave by computing the local power spectrum $P_\eta(\omega)$ of wave height $\eta(t,x_v,y_v)$, using the vibrometer. P_η is defined as the square modulus of the Fourier transform of η and is computed using the pwelch function with MATLAB$^{\text{TM}}$. A typical spectrum for an intermediary amplitudes among the tested one is shown in Fig. 5(a). Peaks corresponding to the mother waves are clearly visible at frequency f_1 and f_2. An additional peak of smaller amplitude is present at the frequency $f_3 = f_1 + f_2$, clearly demonstrating the existence of a mode at f_3. Note here that the amplitude of the daughter wave at f_3 is of the same order of magnitude as the amplitudes of the two harmonics $2f_1$ and $2f_2$. These harmonics are generated by nonlinearity in the generation by the wave makers (typical mother wave steepnesses range: $0.01 < k_i a_i < 0.1$). A peak of smaller amplitude (not depicted) is also observed at $f = f_2 - f_1 = 3$ Hz. Although its generation is also related to a three-wave mechanism, the corresponding wavelength (around 167 mm) is too close to the tank dimensions and we choose to focus on the triad, which is transferring energy at high frequency. Moreover, especially when the forcing amplitude is high enough, higher-order resonant triads are also observable in the spectrum, such as $(f_1,2f_1,3f_1)$, $(f_1,f_1+f_2,2f_1+f_2)$, $(f_2,2f_1,2f_1+f_2)$, (f_2,f_1+f_2,f_1+2f_2), $(f_1,2f_2,f_1+2f_2)$, and $(f_2,2f_2,3f_2)$, which can be seen in Fig. 5(a). At high forcing amplitude, spectral peaks become wider, due to nonlinear broadening. Therefore at high enough forcing the considered triad cannot be taken isolated and we expect a departure from the theoretical considerations of Sec. II B.

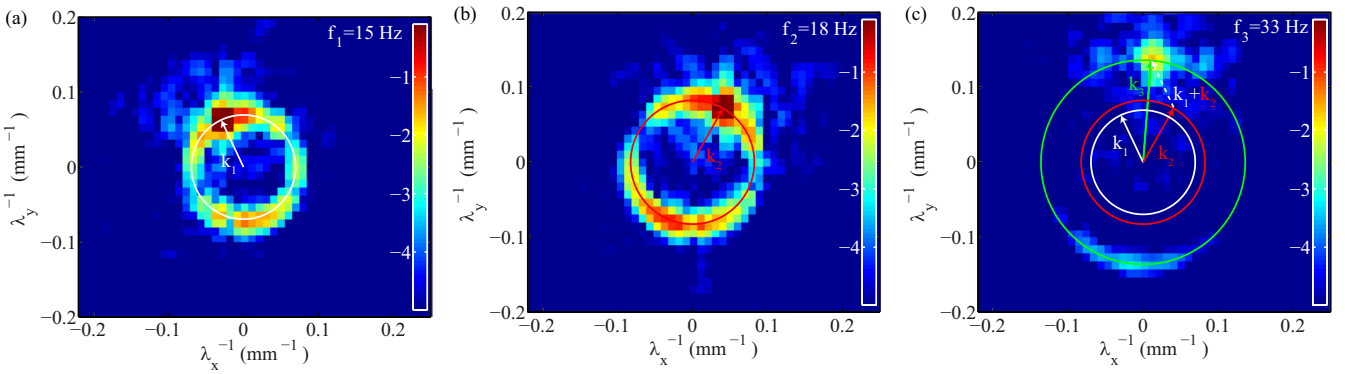

FIG. 6. Spatiotemporal spectra of wave elevation $S_\eta(\omega,k_x,k_y)$, is displayed for the triad frequencies: (a) f_1, (b) f_2, and (c) f_3. Circles correspond to the linear theoretical dispersion relation at the given frequency. The arrows indicate the vector $\mathbf{k_i}$ extracted from the maxima of the experimental spectra. We observe $\mathbf{k_3} \approx \mathbf{k_1} + \mathbf{k_2}$. Color scale $\log_{10}(S_\eta)$ arbitrary unit, with $a_1 = 55$ and $a_2 = 56$ μm.

Using the DLP method, we compute also spatiotemporal power spectra $S_\eta(\omega,k_x,k_y)$ by performing a 2D spatial Fourier transform and a temporal Fourier transform on the wave field $\eta(x,y,t)$. The spectrum $S_\eta(\omega,k)$ with $k = \sqrt{k_x^2 + k_y^2}$ is averaged over the different directions and is displayed in Fig. 5(b), as a function of the inverse of the wavelength λ and of the frequency f. The spatial resolution of the spectrum is equal to $2\pi\,\delta\lambda^{-1} = \delta k \approx 30.5$ m^{-1}. Peaks of the spectrum appear as high amplitude spots. As seen previously, the spectrum contains peaks at the frequencies of the mother waves f_1 and f_2, the harmonics of the mother waves $2f_1$ and $2f_2$ (hardly visible), and the daughter wave $f_3 = f_1 + f_2$. Small amplitude waves are expected to follow the linear gravity-capillary dispersion relation. The experimental dispersion relation can thus be accurately fitted by the linear dispersion relation where the surface tension σ is the only free parameter in Eq. (3). We find here $\sigma_{\text{fit}} = 55$ mN/m, but for other experiments with solution of intralipids σ can be significantly lower, up to 45 mN/m. We observe also a broadening of the relation dispersion in λ^{-1}, evaluated using a Gaussian adjustment of the peaks, as $2\pi\,\delta\tilde{\lambda}^{-1} = \delta\tilde{k} \approx 70$ m^{-1} around the fit. This broadening is due to the finite field of view of the camera, to the weak nonlinearity and to the dissipation of the waves.

B. Verification of the spatial resonance condition

Resonance implies that both temporal and spatial conditions $f_3 = f_1 + f_2$ and $\mathbf{k_3} = \mathbf{k_1} + \mathbf{k_2}$ are satisfied simultaneously. Figure 6 shows separately the spatiotemporal spectra $S_\eta(\omega_i,k_x,k_y)$ for the frequency f_1, f_2, and f_3. In Figs. 6(a) and 6(b), the maximum of each spectrum is observed in the direction of propagation of the wave 1 or 2 at a position from the center equal to $k_i = \|\mathbf{k_i}\|$ given by the linear dispersion relation. However, wave energy is also detected with wave number k_1 and k_2 in other directions than the initial propagation one. Since measurements are performed during the stationary regime, this is due to the multiple reflections on the border of the tank. Despite the multidirectionality observed for the mother waves, for the daughter wave at f_3 in Fig. 6(c), a maximum is clearly detected at $k = k_3$ and the corresponding wave vector $\mathbf{k_3}$ is close to the vectorial sum of $\mathbf{k_1}$ and $\mathbf{k_2}$.

To quantify the verification of the spatial resonance condition, a systematic study was performed for growing mother wave amplitudes. In Fig. 7 for increasing a_1a_2, we

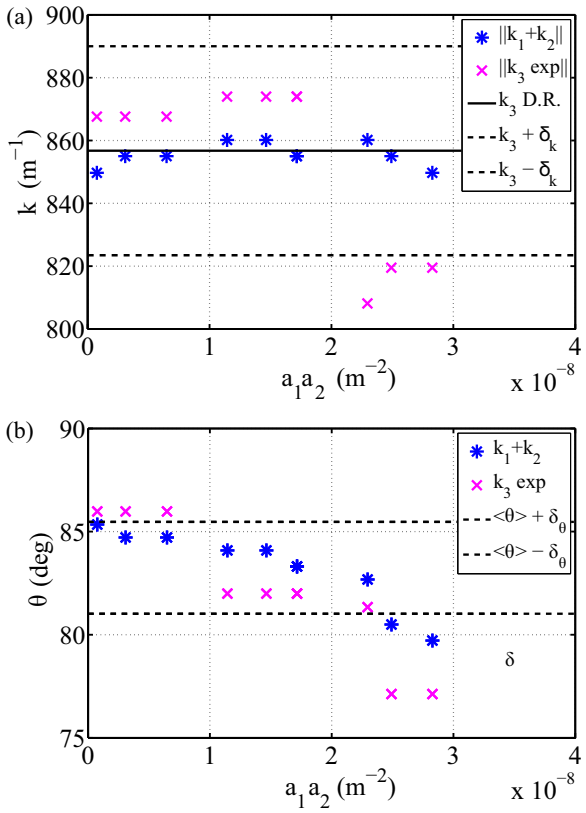

FIG. 7. Comparison between the experimental values of $\mathbf{k_1} + \mathbf{k_2}$ and $\mathbf{k_3}$ exp. as a function of the product $a_1\,a_2$ of the mother wave amplitudes. (a) in norm and (b) in direction, when $\alpha_{12} = 54$ deg. In (a) the value of k_3 given by the linear dispersion relation is represented by a black line. The black dashed line provides the acceptable bounds due to the finite resolution $\delta_k = 30.5$ m^{-1} of the spectra. In (b) θ is the angle between the horizontal axis of Fig. 6(c) and $\mathbf{k_3}$. The black dashed lines indicate the angular accuracy δ_θ around the average orientation $\langle\theta\rangle$ of $\mathbf{k_1} + \mathbf{k_2}$. The product a_1a_2 has been measured with the laser vibrometer, in equivalent experimental conditions.

test the accordance of $\mathbf{k_3}$ with the dispersion relation and on the direction θ made by $\mathbf{k_3}$ with the horizontal axis. As the spectra have a finite resolution $\delta_k = 30.5\ \mathrm{m}^{-1}$, the modulus of $\mathbf{k}$ is measured with an accuracy equal to $\pm\delta_k$ and its direction with an accuracy equal to $\pm\delta_\theta = \delta_k/k_3 = 2.0$ deg. The resonant condition is thus well verified for low values of the product $a_1 a_2$. When this product becomes larger than $2 \times 10^{-8}\ \mathrm{m}^2$ a significant departure is observed, probably due to higher nonlinear effects. The angle θ is also decreasing with the amplitude of the two mother waves. Nevertheless, spatiotemporal measurements show that resonance conditions are well verified in time and space for a significant range of mother wave amplitudes.

C. Spatial behavior of mother and daughter waves

Using the spatiotemporal DLP measurements, we aim to access to the spatial behavior of each component in the triad. Indeed, according to Eq. (10), the daughter wave is expected to grow with the distance and thus its amplitude depends on the spatial coordinate. Moreover, as the system is finite and presents inhomogeneity due to reflections and viscous dissipation, the spatial evolution of the waves has to be studied. To do this, the Fourier power spectrum is applied only in time to the wave field $\eta(x,y,t)$, to obtain a spectrum $S_\eta(x,y,f)$, which is here a function of spatial coordinates and frequency. By taking the spectra for the frequencies f_i in the triad, we can define wave modes $\tilde{a}_i(x,y)$ depicting the spatial distribution of each wave of frequency f_i in the triad. To express $\tilde{a}_i$ as an amplitude, they are obtained by integration of the spectrum around f_i, $\tilde{a}_i(x,y) = \sqrt{2}\left(\int_{f_i-\delta_f}^{f_i+\delta_f} S_\eta(x,y,f_i)\,df\right)^{1/2}$ with $i = 1,2,3$ and $\delta_f = 0.2$ Hz. Note by definition that $\tilde{a}_i$ is averaged with time. Spatial wave modes $\tilde{a_1}$, $\tilde{a}_2$ and $\tilde{a}_3(x,y)$ are plotted respectively in Figs. 8(a)–8(c). Due to the circular boundary of the tank producing a stationary component on the wave field, on each graph we observe a significant modulation at the wavelength $\lambda_i/2$ for the frequency f_i, because the power spectrum is a quadratic operation. Nevertheless, $\tilde{a}_i$ provide a useful evaluation of local wave amplitudes. We observe that the inhomogeneity of the mother wave modes are significant. Nonetheless, in agreement with the results from the spatial spectra, the wave 3 is found to propagate in a direction close to O_y and its amplitude is important in the middle of the crossing region between the two mother wave trains. Then by plotting the amplitudes $\tilde{a}_i$ as a function of the distance d from the bottom of the image, Fig. 9(a), we observe a decay of $\tilde{a}_1$ and $\tilde{a}_2$ due to viscous dissipation and nonlinear pumping by the wave 3. $\tilde{a}_3$ is indeed found to grow slightly. This behavior is qualitatively described with Eq. (10), by taking $\xi \simeq d$. In this equation $a_1 a_2$ is taken as the average value of $\tilde{a}_1\tilde{a}_2$ for $d < 30$ mm. We assume that $\sin\phi = 1$ and we take $v_{g3} = 0.316\ \mathrm{m.s}^{-1}$, $\delta_3 = 4.83\ \mathrm{s}^{-1}$ and so that γ_3 is taken equal to $1.30 \times 10^4\ \mathrm{m}^{-1}$ [see Eq. (8) with the physical properties of the intralipid solution]. Then the origin O at $\xi = 0$ is determined by matching $\tilde{a}_3$ for $d = 0$, which gives $d_0 = -23$ mm. Although $\tilde{a}_3$ is not so small for this measurement and the $\tilde{a}_1$ and $\tilde{a}_2$ are varying in space, the model depicts roughly the a_3 evolution with the good order of magnitude for $d < 50$ mm. At higher distance, inhomogeneity seems too important to make a quantitative comparison.

These results are confirmed for several measurements with different forcing amplitudes by plotting the rescaled amplitude $\tilde{a}_3/(\tilde{a}_1\tilde{a}_2)$ in Fig. 9(b). We observe that the fast spatial modulations are not coherent from one measurement to another, although experiments have been performed successively in identical conditions. We suppose that the stationary pattern of standing waves depends in the capillary regime on the meniscus shape on the border of the circular tank, which is known to be subjected to hysteresis. Except at lowest mother wave amplitudes, where signal to noise ratio is too important and at high amplitude, the rescaled evolution of $\tilde{a}_3$ is in qualitative agreement with the model despite the approximations, which validates the resonant interaction theory. Moreover, we demonstrate that for capillary-gravity waves, neither the linear growth solution [Eq. (12)] nor the saturated solution by viscous dissipation [Eq. (13)] describes the observations and thus the more complete solution [Eq. (10)] has to be used, which is taking into account the spatial growth of a_3 with ξ.

D. Amplitudes and phase locking in stationary regime

After verifying the resonance conditions and showing that Eq. (10) describes the spatial behavior of the daughter wave in stationary regime, we study now its temporal dynamics

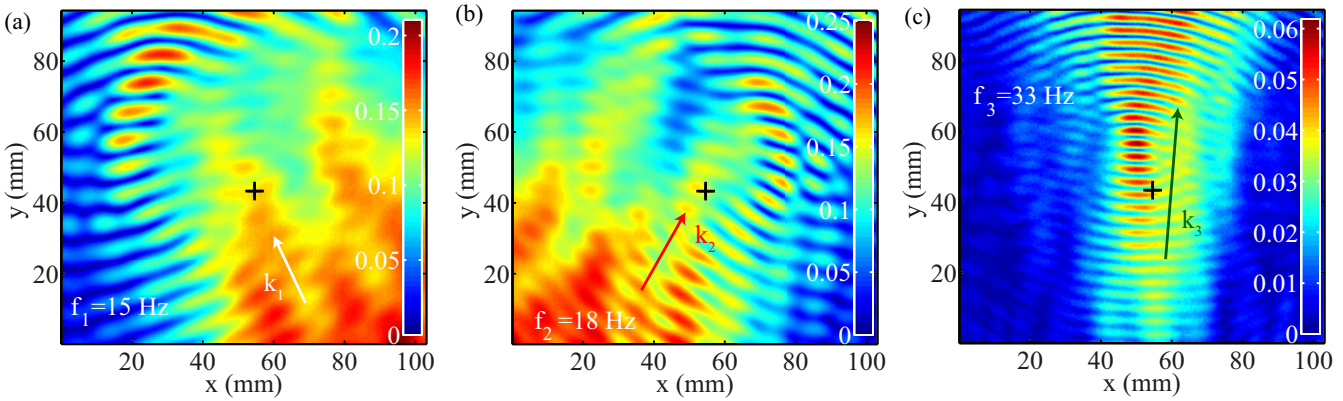

FIG. 8. (a) $\tilde{a}_1(x,y)$ providing the spatial distribution of wave mode at the frequency f_1, when $\alpha_{12} = 54$ deg. The black cross indicates the corresponding position of the laser beam for the measurements performed with the vibrometer. Color scale $\tilde{a}_i$ in mm. Here $a_1 = 104$ and $a_2 = 110\ \mu$m. (b) $\tilde{a}_2(x,y)$ spatial mode at f_2. (c) $\tilde{a}_3(x,y)$ spatial mode at f_3.

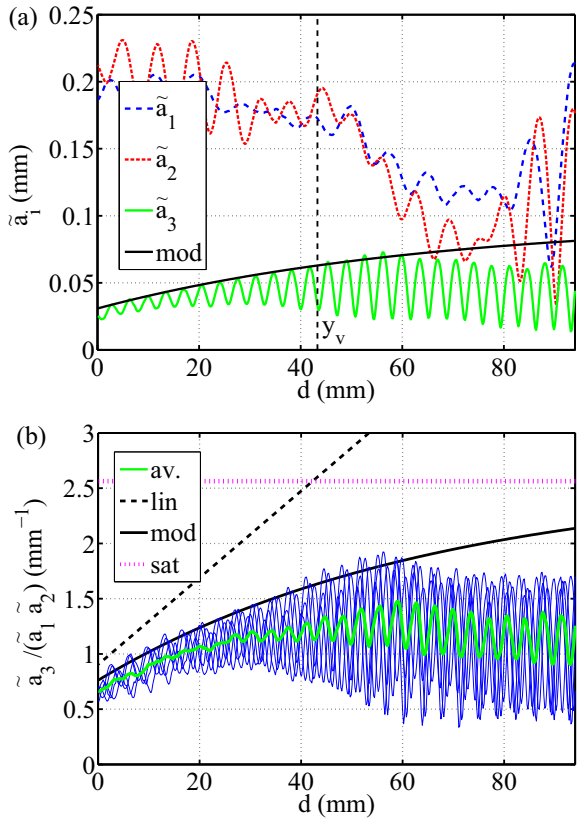

FIG. 9. (a) Evolution of wave amplitudes $\tilde{a}_i$ (averaged between $49 < x < 55$ mm) along the propagation direction of the wave 3 as a function of the distance d from the bottom of the image. The behavior of $\tilde{a}_3$ is compared to the model (black solid line) given by Eq. (10) with $\xi \simeq d$. The vertical black dashed line gives the position y_v of the laser beam for vibrometer measurements. (b) Rescaled amplitude of $\tilde{a}_3/(\tilde{a}_1\tilde{a}_2)$ as a function of the distance d for different measurements ($6.5 \times 10^{-9} < a_1a_2 < 1.7 \times 10^{-8}$ m^2). We notice that the spatial amplitude modulations are not in phase in the different measurements. The average evolution of $\tilde{a}_3$ on the measurements, green (light gray) line, is compared with the model given by Eq. (10), black solid line. The linear limit for negligible dissipation [black dashed line from Eq. (12)] and the saturated value [light-gray dotted line from Eq. (13)] are also depicted.

in more accurate measurements using the laser Doppler vibrometer. Twelve realizations of the same experiment and for 12 increasing mother wave amplitudes have been performed. Concerning the experimental protocol, at $t = 10$ s, excitation is started for 150 s and is then stopped at $t = 160$ s, whereas wave heights are recorded during the total duration of the experiment lasting 170 s.

From the measurements, we examine the evolution of the amplitudes and the phases of the different components of the triad in the stationary regime at the position (x_v, y_v). To do so, the vibrometer signal is filtered around each considered frequency f_i: the filter is of Butterworth type, of order 2 and with a pass band of $2\Delta f$ ($\Delta f = 0.5$ Hz). Resulting signals are then integrated over time, to transform vertical interface velocity into wave amplitudes. Then a Hilbert transformation is applied to the signal in order to extract separately the instantaneous wave amplitude $a_i(t)$ and the instantaneous phase $\psi_i = \mathbf{k_i} \cdot \mathbf{x}_v - \omega_i t + \phi_i$ of the different waves at the laser beam position $\mathbf{x}_v$.

Looking at the amplitudes a_i averaged on 12 realizations in Fig. 10(a), we can see that after a transient and a small overshoot, the amplitudes stabilize to a stationary value. At $t = 160$ s, when the excitation is stopped, the amplitudes return to zero. The growing and decaying transient regimes involve shaker dynamic response, wave propagation, viscous dissipation, and nonlinear wave interaction. Due to the lack of temporal resolution resulting from the filtering operation, transients cannot be used to evaluate the growth coefficient γ_3 of the daughter wave. We notice also that the amplitude of the daughter wave, around 20 μm, is smaller than the amplitudes of the mother waves, around 130 μm ($a_3 \ll \sqrt{a_1\, a_2}$).

Concerning the phase, Fig. 10(b) displays $\sin\phi$ as a function of t. If the resonant conditions of Eq. (4) are verified, by computing $\psi_1 + \psi_2 - \psi_3$, we obtain the total phase $\phi = \phi_1 + \phi_2 - \phi_3$ and so the $\sin\phi$ term involved in Eq. (6). During the transient regimes, phases ϕ_i are not related and $\sin\phi$ fluctuations are fast. Then, once stationary regime is reached, $\sin\phi$ evolves slowly and stabilizes to 1. Therefore, there is a constant relation between the phases in the triad, i.e., a phase locking around $\phi = \pi/2$ as expected theoretically to have a stationary phase behavior [see Eq. (7)]. This constitutes a strong argument proving that the wave 3 is created by the resonant interaction mechanism.

The influence of increasing the amplitudes of the two mother waves is presented in Figs. 10(c) and 10(d) for which both amplitudes a_i and $\sin\phi$ are averaged first over time in the stationary regime (between $t = 60$ and 140 s) and then on the 12 consecutive identical experimental realizations. In these experimental conditions, Fig. 10(c) shows the mean value and the standard deviation of $\sin\phi$ versus a_1a_2. Except at the lowest amplitudes, standard deviation of $\sin\phi$ is quite small (below 0.02), showing that a phase locking occurs. But we observe that the phase locking value differs at small amplitude from the expected value of 1. Figure 10(d) presents the evolution of $a_3\delta_3/[K(\xi)\sin\phi]$ versus a_1a_2. As expected from Eqs. (10) and (11), we found a proportional behavior between the rescaled a_3 and a_1a_2, at least for not too high amplitudes. Following Eq. (10), we estimate the interaction coefficient γ_3 for the daughter wave by computing the slope of the linear fit of $a_3\delta_3/[K(\xi)\sin\phi]$. To take into account the growth of the daughter wave on a distance ξ between the beginning of the wave train and the laser spot, the coefficient $K(\xi)$, has to be evaluated. For these experiments the distance ξ is roughly 30 mm, leading to $K(\xi) = 0.33$. The slope of the linear fit in Fig. 10(d) is 4.85×10^3 m^{-1}.s^{-1}, and gives, thus, an estimate of γ_3. We obtain, thus, an experimental estimation of the nonlinear interaction coefficient $\gamma_{3\text{exp}} = 1.46 \times 10^4$ m^{-1}.s^{-1}, which is 20% more than the theoretical value $\gamma_3 = 1.24 \times 10^4$ m^{-1} s^{-1}. Note that repeating the experiments with another triad (16, 23, 39) Hz leads to an estimation of the coefficient $\gamma_{3,\text{exp}} = 1.22 \times 10^4$ m^{-1} s^{-1}, which is 13% less than the theoretical value $\gamma_{3,th} = 1.41 \times 10^4$ m^{-1} s^{-1}.

These measurements validate, thus, the generation of a daughter wave from the interaction between two mother waves, for capillary-gravity waves in a closed tank. It is important to keep in mind that the wave field presents inhomogeneity for two main reasons: first, the presence of a significant standing

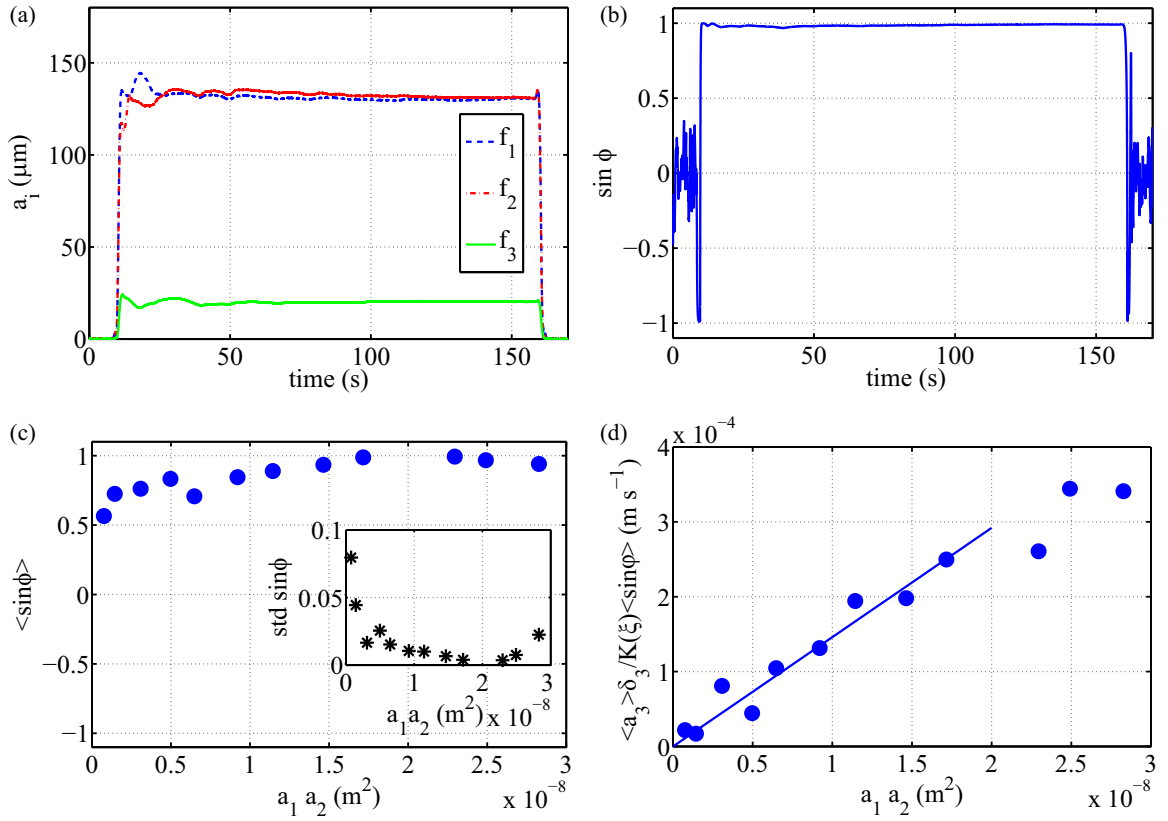

FIG. 10. (a) Amplitudes a_i and (b) $\sin\phi$ versus time for $f_1 = 15$ Hz, $f_2 = 18$ Hz, and $\alpha_{12} = 54$ deg. For these parameters, $a_1 = 130$ and $a_2 = 132$ μm. (c) Mean value of $\sin\phi$ versus a_1a_2 in stationary regime, with in the inset: the standard deviation of $\sin\phi$, quantifying fluctuations around the mean value. We observe that the phase locking occurs for the considered forcing amplitudes, but at low forcing $\sin\phi$ departs slightly from 1 and fluctuations are stronger. (d) In stationary regime $\langle a_3\rangle \times \delta_3/(K(\xi)\langle\sin\phi\rangle)$ is found proportional to a_1a_2 for small and moderate forcing. Solid line is the linear fit valid for not too high values of a_1a_2.

wave part, in addition to the main propagative part; second, the viscous dissipation decreases significantly the amplitudes of the mother waves as they propagate away from the wave makers. Moreover, the frequencies f_1, f_2, and f_3 of the triad, are involved in other nonlinear mechanisms. Nevertheless, the main features given by the resonant interaction theory are recovered in this experiment. We observe that the daughter wave verifies the resonant conditions in frequency and wave number. Furthermore, the total phase ϕ is locked to a value close to $\pi/2$. The nonlinear interaction coefficient experimentally estimated is finally quite close to the theoretical one, considering that the experimental conditions are not strictly conform to the framework of the theory.

V. CONCLUSIONS AND DISCUSSION

We report an experimental study on three-wave interactions of capillary-gravity waves in a closed tank. We showed that the interaction between two mother wave trains at frequencies f_1 and f_2 creates a daughter wave at $f_3 = f_1 + f_2$. For mother waves crossing at the resonant angle, we experimentally validate the three-wave resonant mechanism. By means of a spatiotemporal measurement, we verify that the spatial resonance condition is fulfilled. We also observe a phase locking at $\phi = \pi/2$, between the different waves of the triad as theoretically expected. In the stationary regime, we measure the growth rate of the daughter wave amplitude a_3, which is found to be proportional to $\gamma_3\, a_1a_2$, with a_1 and a_2 the mother wave amplitudes. Our quantitative estimation of the nonlinear interaction coefficient γ_3 gives the correct order of magnitude with respect to the theoretical value, within an accuracy of less than 20%. This extensive study has been performed for two different triads (15, 18, 33) Hz or (16, 23, 39) Hz (the latter is not shown here). Similar results are found. This confirms that the features of three-wave interaction reported here can be generalized to different capillary-gravity triads within a frequency range of approximatively $10 < f < 50$ Hz.

Several phenomena could be addressed to explain the slight departures between experimental and theoretical values: (i) higher-order interactions at high forcing amplitude; (ii) wave reflections on the boundary of the tank producing standing waves, which reduce the homogeneity of the wave field where the daughter wave is studied; (iii) issues to localize the beginning of the daughter wave in local measurements; and (iv) finite width of the wave trains that could also modify the derivation of interaction coefficients [41].

The model used here [Eqs. (6), (7), and (10)], involving viscous dissipation as a perturbation [2,29,33], describes appropriately our results in the stationary regime. The characteristic nonlinear time τ_{nl} for the growth of a_3 can be approximated as $1/\tau_{nl} = (\gamma_3\sqrt{a_1a_2})$. For the triad (15,18,33) Hz, $1/\tau_{nl} \approx 1.24$ s^{-1} taking $a_1a_2 \approx 1.10^{-8}$ m^2 [Fig. 10(d)], leading to

$\tau_{nl} \approx 0.81$ s. The dissipative time is evaluated as $\tau_d = 1/\delta_3 = 0.23$ s. For capillary waves, the dissipation is thus always too strong to be neglected and it is surprising that inviscid theories provide correct values for the interaction coefficients. Consequently, a theoretical effort describing three-wave resonant interactions from Navier-Stokes equations for surface waves, would be of prime interest.

Note that such an extensive experimental study of three-wave interaction for gravity-capillary waves on the surface of a fluid has never been tested, although this process transfers energy at small scale in wave turbulence. Indeed, previous works using only collinear wave trains investigated the degenerated case of Wilton ripples [29,30] or the subharmonic generation where one wave at high frequency produces two waves at a lower frequency [31–33]. Here, we emphasized that for a given couple of mother wave frequencies the resonance conditions impose, theoretically from Eq. (5), the value of the resonant angle between the two mother waves. When the angle is experimentally fixed to the resonant angle, we have shown here that three-wave interactions are correctly described by the resonant interaction theory. As these interactions are the elemental mechanism of capillary wave turbulence, this study seems to show that resonant interactions ensure energy transfer through the scales. The average flux ϵ_3 transferred to the daughter wave by unit of area and density, can be estimated from the energy of the wave 3 [42]. After spatial and temporal averaging, we find $\langle \epsilon_3 \rangle \approx 2 \times 10^{-7} \mathrm{m}^3\,\mathrm{s}^{-3}$, which is close to values obtained in capillary wave turbulence experiments in water, when energy flux is evaluated through the dissipated power [26]. Nevertheless, it is important to evaluate and understand the relative contribution of three-wave quasiresonances [36] and nonresonant interactions [6] in front of the resonant interactions for gravity-capillary wave experiments in laboratory.

ACKNOWLEDGMENTS

The authors thank the Agence Nationale de la Recherche (Grant No. ANR-12-BS04-0005), which funded this work. We acknowledge also C. Laroche for technical assistance.

APPENDIX: ATTENUATION OF THE WAVES DUE TO VISCOUS DAMPING

In our experiments, the amplitude of a daughter wave is due to a balance between viscous attenuation and three-wave interactions. In order to experimentally determine the viscous dissipation or attenuation coefficients δ_i, we have performed experiments with only one wave maker generating a monochromatic wave, with f_1, f_2, and f_3 generated separately. The amplitude of the wave has been recorded every centimeter with the laser vibrometer put on a linear translation stage. A beach with a slope around 45 deg and lateral walls has been placed in the tank in order to avoid reflections of the waves when encountering the solid curved walls of the tank.

The evolution of amplitude is expected to decrease exponentially with the distance from the wave maker. For a given frequency, the attenuation length l_i can be estimated from the decaying exponent of an exponential fit performed on the experimental amplitudes as shown in Fig. 11, for

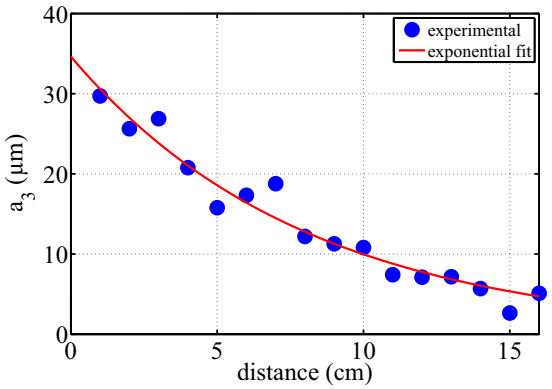

FIG. 11. Decrease of the amplitude of the wave with frequency $f = 33$ Hz versus the distance from the wave maker, for a small excitation forcing amplitude.

a frequency equal to 33 Hz. Then the coefficients δ_i are simply computed by $\delta_i = v_{gi}/l_i$. The group velocities are calculated using $v_{gi} = \partial\omega_i/\partial k_i$ for deep water dispersion relation, $\omega_i = \sqrt{gk_i + \frac{\sigma}{\rho}k_i^3}$. This leads to:

$$\partial\omega_i/\partial k_i = \frac{1}{2}\left(g + \frac{3\sigma}{\rho}k_i^2\right)\left(gk_i + \frac{\sigma}{\rho}k_i^3\right)^{-1/2}. \qquad \text{(A1)}$$

Despite the experimental care in preparing the solution of TiO_2, the dissipation exponents are found after one hour, well described by the inextensible free-surface model due to the presence of insoluble surfactants [25,43–45]. The values of the viscous dissipation coefficients are thus computed using the formula $\delta_{i\,\mathrm{model}} = \sqrt{2}\sqrt{\nu\omega_i}k_i/4$. The values of the norms of the wave vectors k_i (found with the graphical resolution of Fig. 1(b) with $\sigma = 60$ mN/m), the phase and group velocities v_{pi} and v_{gi}, the attenuation parameters $\delta_{i\,\mathrm{model}}$, l_i, and δ_i are reported in Tables II and III. Note that the measured coefficients are close to the value of $\delta_{i\,\mathrm{model}}$ (maximum relative error around equal to 7%).

Note, as previously mentioned, that gravity-capillary waves are sensitive to the contamination of the surface, which is an unavoidable effect. In order to check if contaminants play a significant role in the present experimental conditions we have performed, for an arbitrary angle between the two wave makers, a complete series of experiments with a home-built plastic cover and the same series another day without the

TABLE II. Norms of the wave vectors, phase, and group velocities. The different values are calculated with $\sigma = 60$ mN/m and $\rho = 1000$ kg m^{-3}.

	k_i (m^{-1})	v_{pi} (m s^{-1})	v_{gi} (m s^{-1})
$f_1 = 15$ Hz	428	0.220	0.227
$f_2 = 18$ Hz	507	0.223	0.248
$f_3 = 33$ Hz	834	0.249	0.326
$f_1 = 16$ Hz	455	0.221	0.234
$f_2 = 23$ Hz	626	0.231	0.278
$f_3 = 39$ Hz	946	0.259	0.349

TABLE III. Viscous damping coefficients (viscous model: $\delta_{i\,\mathrm{model}} = \sqrt{2}\sqrt{\nu\omega_i}k_i/4$), experimentally measured attenuation lengths and corresponding deduced viscous damping coefficients. The different values are calculated with $\sigma = 60$ mN/m.

	$\delta_{i\,\mathrm{model}}$ (s^{-1})	l_i (m)	δ_i (s^{-1})
$f_1 = 15$ Hz	1.49	0.162	1.40
$f_2 = 18$ Hz	1.93	0.128	1.94
$f_3 = 33$ Hz	4.31	0.080	4.07
$f_1 = 16$ Hz	1.63	0.122	1.92
$f_2 = 23$ Hz	2.70	0.103	2.70
$f_3 = 39$ Hz	5.31	0.061	5.71

plastic cover. Results appear to be comparable with and without the cover, except during the first hour.

Finally, viscous damping coefficient have been also measured for the solution of intralipids using the DLP method. Spatial decay of sinusoidal wave trains are found compatible with the inextensible free-surface model, $\delta_{i\,\mathrm{model}} = \sqrt{2}\sqrt{\nu\omega_i}k_i/4$. Compared to the solution of TiO_2, this solution has a lower surface tension $\gamma = 55\,\mathrm{mN\ m^{-1}}$ and a slightly higher viscosity $\nu = 1.24\,\mathrm{m\ s^{-2}}$. We obtain this, for example, for $f_3 = 33$ Hz, $v_{g3} = 0.316\,\mathrm{m\ s^{-1}}$ and $\delta_3 = 4.83\,\mathrm{s^{-1}}$. Therefore, both liquids used in this experimental study have analogous physical properties and we observe the same behavior for the three-wave resonance mechanism.

[1] O. M. Phillips, J. Fluid Mech. **106**, 215 (1981).
[2] A. D. D. Craik, *Wave Interactions and Fluid Flows* (Cambridge University Press, Cambridge, 1986).
[3] J. L. Hammack and D. M. Henderson, Annu. Rev. Fluid Mech. **25**, 55 (1993).
[4] O. M. Philipps, J. Fluid Mech. **9**, 193 (1960).
[5] M. S. Longuet-Higgins, J. Fluid Mech. **12**, 321 (1962).
[6] P. Janssen, *The Interaction of Ocean Waves and Wind* (Cambridge University Press, New York, 2004).
[7] L. F. McGoldrick, J. Fluid Mech. **21**, 305 (1965).
[8] F. K. Ball, J. Fluid Mech. **19**, 465 (1964).
[9] R. W. Boyd, *Nonlinear Optics* (Academic Press, Berlin, 2008).
[10] S. Joubaud, J. Munroe, P. Odier, and T. Dauxois, Phys. Fluids **24**, 041703 (2012).
[11] G. Bordes, F. Moisy, T. Dauxois, and P.-P. Cortet, Phys. Fluids **24**, 014105 (2012).
[12] V. Sokolov and A. K. Sen, Phys. Rev. Lett. **113**, 095001 (2014).
[13] L. Deike, M. Berhanu, and E. Falcon (unpublished).
[14] V. E. Zakharov, V. L'vov, and G. Falkovich, *Kolmogorov Spectra of Turbulence* (Springer-Verlag, Berlin, 1992).
[15] S. Nazarenko, *Wave Turbulence* (Springer-Verlag, Berlin, 2011).
[16] S. Nazarenko, S. Lukaschuk, S. McLelland, and P. Denissenko, J. Fluid Mech. **642**, 395 (2010).
[17] L. Deike, B. Miquel, P. Gutiérrez, T. Jamin, B. Semin, M. Berhanu, E. Falcon, and F. Bonnefoy, J. Fluid Mech. **781**, 196 (2015).
[18] E. Falcon, C. Laroche, and S. Fauve, Phys. Rev. Lett. **98**, 094503 (2007).
[19] W. B. Wright, R. Budakian, and S. J. Putterman, Phys. Rev. Lett. **76**, 4528 (1996).
[20] E. Henry, P. Alstrom, and M. T. Levinsen, Europhys. Lett. **52**, 27 (2000).
[21] M. Brazhnikov, G. Kolmakov, A. Levchenko, and L. Mezhov-Deglin, Europhys. Lett. **58**, 510 (2002).
[22] C. Falcón, E. Falcon, U. Bortolozzo, and S. Fauve, Europhys. Lett. **86**, 14002 (2009).
[23] H. Xia, M. Shats, and H. Punzmann, Europhys. Lett. **91**, 14002 (2010).
[24] M. Berhanu and E. Falcon, Phys. Rev. E **87**, 033003 (2013).
[25] L. Deike, M. Berhanu, and E. Falcon, Phys. Rev. E **85**, 066311 (2012).
[26] L. Deike, M. Berhanu, and E. Falcon, Phys. Rev. E **89**, 023003 (2014).
[27] K. M. Case and S. C. Chiu, Phys. Fluids **20**, 742 (1977).
[28] W. F. Simmons, Proc. R. Soc. A **309**, 551 (1969).
[29] L. F. McGoldrick, J. Fluid Mech. **40**, 251 (1970).
[30] Y. Y. Kim and T. J. Hanratty, J. Fluid Mech. **50**, 107 (1971).
[31] P. Banergee and A. Korpel, Phys. Fluids **25**, 1938 (1982).
[32] S. Hogan, Phys. Fluids **27**, 42 (1984).
[33] D. M. Henderson and J. L. Hammack, J. Fluid Mech. **184**, 15 (1987).
[34] M. Perlin, D. Henderson, and J. Hammack, J. Fluid Mech. **219**, 51 (1990).
[35] M. Perlin and J. Hammack, J. Fluid Mech. **229**, 229 (1991).
[36] Q. Aubourg and N. Mordant, Phys. Rev. Lett. **114**, 144501 (2015).
[37] H. Punzmann, M. G. Shats, and H. Xia, Phys. Rev. Lett. **103**, 064502 (2009).
[38] M. S. Longuet-Higgins and N. Smith, J. Fluid Mech. **25**, 417 (1966).
[39] L. F. McGoldrick, O. Phillips, N. Huang, and T. Hodgson, J. Fluid Mech. **25**, 437 (1966).
[40] A. Przadka, B. Cabane, V. Pagneux, A. Maurel, and P. Petitjeans, Exp. Fluids **52**, 519 (2012).
[41] B. Bourget, H. Scolan, T. Dauxois, M. Le-Bars, P. Odier, and S. Joubaud, J. Fluid Mech. **759**, 739 (2014).
[42] The energy per surface unit of each triad component can be expressed as $E_i(t) = \frac{1}{2}\rho\omega_i\, v_{pi}\, a_i^2(t)$, with v_{pi} the phase velocity of the wave i [28].
[43] H. Lamb, *Hydrodynamics* (Springer-Verlag, Berlin, 1932).
[44] W. van Dorn, J. Fluid Mech. **24**, 769 (1966).
[45] D. Henderson and H. Segur, J. Geophys. Res., [Oceans] **118**, 5074 (2013).